Detailled structure of the Hengill geothermal volcanic complex, Iceland inferred from 3-D tomography of high-dynamic broadband seismological data

Philippe Jousset

BRGM - ARN

3 Avenue Claude Guillemin - BP6009

45060 Orleans Cedex 02, France

p.jousset@brgm.fr

Christian Haberland and Klaus Bauer

Geoforschung GeoZentrum Potsdam

Knutur Arnasson

Iceland Geosurvey

September 5, 2008

To be submitted to Geothermics

Preliminary manuscript - DRAFT

Abstract

Structural features of geothermal systems allow us to infer location of productive areas before drilling. We use observations high-dynamic intrument broad-band seismological records to perform a detailled tomography at Hengill volcanic triple-junction complex and geothermal system. This well developed geothermal system is exploited to extract hot vapour which is used for electrical power and heat production, and new wells have been drilled to increase the power supply. In order to improve our understanding of the relationships between seismic activity and vapour production, a seismological network including 5 broadband instruments (120 s - 50 Hz) and 2 broadband instruments (60 s - 50 Hz) was setup from June 26th, 2006 till October 17th, 2006, at the Hengill geothermal system, in the framework of the I-GET project (European Commission FP6 programm). In addition, we included continuous seismic data from 3 permanent stations of the SIL network. Data analysis allowed us to detect automatically and classify semi-automatically more than 600 earthquakes, amongst which long-period (LP) earthquakes were observed for the first time in this area. We used more than 260 local volcano-tectonic earthquakes with clear P- and S- arrival times to perform a simultaneous inversion for the 3-D velocity structure and the hypocenter determination. Results give us more insights than previously obtained in this area, especially on the existence of a high velocity anomaly, that we correlate with a resistivity anomaly, in the area of Olkelduhals from about 2 to 4 km depth and a low v_P/v_S ratio anomaly beneath the northern part of Mt. Hengill below 4-5 km. We discuss possible interpretations and implications of those observations.

Keywords: broadband seismology, seismic tomography, fluid, geothermy, Hengill volcano.

1 Introduction

Hydrothermal systems offer a non-polluting long-term alternative as energy supply (Barnea, 1972). The exploitation of geothermal energy is limited at present, because drilling exploration wells is expensive, and hydrothermal systems are often associated with volcanic and seismic activity, which may put geothermal exploitation at risk (Ward, 1972). In order to reduce the risk of dry-drilling, the structural features of the targeted geothermal system is a critical knowledge prior to drilling. Amongst the cheapest geophysical methods to infer the crustal structure, passive seismology is of first choice. Both classical local seismic tomography in those areas where local seismicity is numerous (Benz et al., 1996), and newly developed surface wave tomography techniques applied to ambiant noise have been shown able to image detailled crustal subsurface structure (Brenguier et al., 2007).

Recently developed broadband seismometers allow the acquisition of broadband signals, like long-period (LP) earthquakes (0.5 s to 5 s) and tremor and very-long-period (VLP) earthquakes (above 5 s), having specific characteristics described mainly in terms of duration and frequency content. These signals have been observed at many active volcanoes (Neuberg et al., 1994, e.g), hydrothermal systems and also oil fields (Dangel et al., 2003). We applied these techniques to a data set from a temporary broadband seismological network of 7 broadband seismic stations set up at Hengill volcano area, Iceland. The two main objectives are three-fold:

1. To record passive seismicity associated with the Hengill volcanic complex, in relation with the exploitation of the geothermal system, especially within the LP earthquake frequency band (< 5 Hz) and relate the seismicity to the known structural features of the geothermal system;

2. To improve our knowledge of the 3-D structure of the exploited geothermal system, by using local seismic tomography inversion techniques, with microearthquakes recorded by the network. Previous tomography studies carried out at Hengill (e.g Toomey and Foulger, 1989), reveal the main structural feature of

the volcanic area and the triple junction, but they are not sufficiently detailed for a detailed analysis of the structural feature of the geothermal system itself. In particular, the v_P/v_S ratio and attenuation measurements are very diagnostic of pore-fluid and temperature conditions when used in conjunction with v_P (Evans et al., 1994), in relation with the non-double couple earthquakes.

3. To analyse the frequency content of the seismicity, especially that of non-double couple events (Miller et al., 1998), thought to be possible signatures of fluids movements linked to the exploitation and relate them to LP earthquakes (Chouet, 1996). Note that an improvement in the velocity model accuracy is required in order to locate and inverse for source mechanism of LP earthquakes (Lokmer et al., 2007).

In the present paper, we focus on the two first objectives set above, i.e., by performing a seismic tomography to improve the resolution of structural features within the geothermal field. After we give elements on Hengill geological setting in Section 2, we describe data acquisition and processing in Section 3. We explain then our strategy to perform the tomography inversions in Section 4, and finally we discuss results in Section 5. The theory and method of local tomography inversion has been described in detail by a number of authors (e.g., Thurber, 1983; 1986; 1993; Kissling, 1988; Ellworth et al., 1991; Eberhart-Phillips, 1993; Iyer and Hirahara, 1993; Ellworth et al., 1994; Eberhart-Phillips and Michael, 1998; Tryggvason et al., 2002; Koulakov et al., 2007). Details of tomographic method with equations with resolution and spread function are given in the appendix A. We use 341 microearthquakes with clear compressional $P-$wave and shear $S-$ wave arrival times to image the structure of the geothermal reservoir applying tomographic inversion to 2266 $P-$ and 2432 $S-$ arrival times with the computer program *SIMULPS12* (Evans et al., 1994), which solves simultaneously for earthquake locations and crustal structure by the iterative damped-least-square method. The program *VELEST* (Ellworth et al., 1994) provides one-dimensional v_P (and v_S) models used as a starting point for the inversion. A careful choice on the earthquakes and inversion parameters has been done prior to the inversion (Eberhart-Phillips, 1993).

2 The geothermal field at Hengill volcano within the tripple junction tectonic setting

2.1 Geological setting of Hengill Volcano Complex

The existence of a large geothermal anomaly at Hengill volcanic systems comes from its specific location within the geodynamical context of Iceland (Ingolfsson et al., 2008). Hengill volcanic systems are located at the crossing of three tectonic systems:

(1) the Reykjanes Peninsula, which is the aerial expression of the Reykjanes Ridge spreading between North America plate and Europe plate to the South;

(2) the West Volcanic Zone - spreading between the two former plates to the North, and

(3) the South Island Seismic Zone - transform zone to the EVZ to the East. This makes this area a tripple junction, favorable to the rising of magma and heat pulses from depth (Foulger, 1995).

An intense fissure swarms crosses Mount Hengill (Figure 1) and extends from the coast south to Hengill and to north of Lake Thingvallavatn. At the Eastern edge of Hengill volcanic system, there is a second volcanic production system called Hrómunddartindur, and a third volcanic system Grensdalur is located to the south.

2.2 The geothermal system of Hengill Volcano Complex

Knutur, please verify and adjust this paragraph

Hengill Tripple Junction system was found in the late sixties to have high potential for vapour and geothermal energy production centers (Gunnarsson et al., 1992). The natural geothermal activity is expressed as numerous hot springs and fumaroles that occur widespread in the area around three central volcanoes

(Hengill, Hrómunddartindur and Grensdalur volcanoes), covering an area of 70 km^2 (Saemundsson, 1995; Arnórsson et al., 2008). The heat loss is about 350 MW. An estimate of the order of magnitude of the total recoverable heat resources in the Hengill area based on the reservoir model (Bödvarsson, 1970), indicated a total of the order of 1010 tons of water at 220 to 230 degrees C could be produced for about 100 years.

The Hengill geothermal system, where the exploration targets for steam and hot water for electricity generation and space heating, is mainly located in volcanic centres, within a fissure swarm of the rift zone is characterised by both porous and fissure oriented anisotropic permeability.

The Nesjavellir geothermal power plant (Figure 1) is one of the first power plant set up to produce geothermal power in 1986 after extensive exploration studies (Gunnarsson et al., 1992). There, over 20 wells up to 2.5 km deep have been drilled. The Heilliheidi is a recent area where wells have been drilling in 2006. The geothermal activity of Hromunddartindur is the most intense in the South of the edifice at lkelduhls, and new wells have been drilling since 2000.

Even if knowing the precise location of the highest geothermal potential is not very critical in this area (90 % of wells are productive when drilled!), Hengill geothermal system structure is one of the best studied, and may be seen therefore as a natural laboratory to test new exploration techniques, like broadband seismology, and to improve our knowledge about Hengill geothermal system as well, as questions remain unsolved (Tryggvason et al., 2002), i.e., possible existence of partial melt or/and supercritical fluid at depth. At present, geothermal fluids are mined at the depth of about 2 km, but the ongoing Iceland Deep Drilling Project (IDDP) aims at extracting supercritical fluids from the depth of about 4 km.

2.3 Seismicity at Hengill volcano

The recent tectonic activity is bound to the to the Hengill volcanic system, since the center of volcanic productions has shifted from Grensdalur to the Hengill sys-

tem some 0.5 Ma ago. Apart from a small eruption in 1789 at Hengill volcano, which accompanied the last rifting episode, the last major eruption occurred about 2000 years ago. Between 1952 and 1955, several earthquake swarms occured in the Hengill area and ended with a magnitude 5.5 event in 1955 (Rögnvaldsson et al., 1998). In 1994, intense swarm activity started at Hengill area beneath Hrómunddartindur volcano, with several thousands events above magnitude 0.5, recorded by the South Iceland Lowland (SIL) network (Stefánsson et al., 1993; Jakobsdóttir, 2008). In March 1995, the activity spread to Ölfus area, about 10 km south of the Hengill and Hrómunddartindur volcanoes. This activity stopped in mid 1996; a second sequence started in 1997 which culminated with 2 magnitudes 5.5 earthquakes in June and November 1998. Mid-1999, the activity returned to the pre-1994 level. Repeated geodetic measurements detected uplift (a few millimeters) and expansion between 1986 and 1995 in the South-East area of Hengill volcano (Sigmundsson et al., 1997; Feigl et al., 2000). This activity is interpreted as a small magma intrusion at a depth of about 7 km, inducing about 90000 earthquakes. This large number of earthquakes for a small intrusion is explained by the low background stress level: this intrusive event present the lowest increase in stressing rate measured in connection with a magma intrusion in Iceland, but produced the most persistent recorded Icelandic seismic swarms (Pedersen et al., 2007).

Cooling, mostly due to natural heat loss, and consequential thermal contraction and cracking in the heat source, are thought to be responsible for the continuous small-magnitude earthquake activity in this area (Miller et al., 1998). This mode of earthquake induction was suggested following the observation that many of the earthquakes have merely non-double-couple focal mechanisms with large explosive components (Foulger and Long, 1984). The mechanism responsible for those non-double-couple may be fluid flow into newly formed cracks (Miller et al., 1998; Sens-Schönfelder et al., 2006).

The structure of the Hengill region has been studied using geological and tectonic and seismological 3-D tomography techniques by a number of authors (Foulger, 1988a; Foulger and Toomey, 1989; Foulger et al., 1995; Saemundsson,

1995; Evans et al., 1996; Julian et al., 1997; Miller et al., 1998; Tryggvason et al., 2002), together with analysis of earthquake source mechanism (Foulger and Long, 1984; Foulger, 1988b; Foulger et al., 1989; Miller et al., 1998) or analysis of swarms (Sens-Schönfelder et al., 2006).

In 1981, a temporary network of 23 analog seismic stations with vertical component seismometers recorded 2000 locatable earthquakes (Foulger, 1988a; 1995), from which a 3-D variation of compressionnal-wave speed v_P was obtained (Toomey and Foulger, 1989; Foulger and Toomey, 1989) with a resolution of 2 km horizontaly and 1 km vertically. The major structural features found are high-v_P bodies at depths ranging 0 to 4 km around Hengill volcano, whereas a small (about 5 km^3) low velocity (about -7 %) was found beneath the northern edge of Mount Hengill, interpreted as a small volume of partial melt (Foulger, 1995).

In 1991, a temporary network of 30 seismic stations with Mark Products L22D 2 Hz, three-component sensors and REFTEK data loggers recorded ground motion continuously with a sampling rate 100 Hz for two months. 4000 earthquakes were recorded. Inversion of 228 well-distributed earthquakes and one explosion allowed (Foulger, 1995; Miller et al., 1998) to apply seismological tomographic methods. In this case, the analysed volume was 3 times larger than the volume analysed in 1981, but the resolution was not improved. Results from this second data set, either inverted together with the first data set or separatelly led to the same final structural features: v_P varies laterally by -10% to +12% from its average value within each layer. No major low v_P body were imaged. The v_P/v_S ration varies by +/-4% throughout the area. The most coherent anomaly involves low v_P/v_S at 0 to 2 km depth, and correlates with areas of hot springs and fumaroles. The low-v_P anomaly beneath the northern part of Mt. Hengill was not detected in the second inversion so its existence was questioned.

Tryggvason et al. (2002) used 9 years of the SIL records (Jakobsdóttir, 2008) comprising about 75000 earthquakes to perform the tomography of Southwest Iceland, with special interest at Hengill triple junction. Their results suggest that both P- and S- waves velocities are drastically reduced beneath the striking

fissure swarm in the Hengill area, with velocities ranging 5.9-6.3 $\mathrm{km\,s^{-1}}$ and 2.4-3.7 $\mathrm{km\,s^{-1}}$, respectively. A low v_P/v_S ratio anomaly is also found, but its location is not accurate, as SIL stations are sparsely set-up around the Hengill geothermal area. On the basis of rock physics estimations (Norris, 1985), the interpretation of these observations is the presence of supercritical fluids rather than a large partly molten rock body. The resolution of the model is 4*4 km.

These studies reveal the main structures of the volcanic area and the tripple junction at Hengill, but the resolutions are not sufficient for inferring details of the geothermal field suitable for drilling. In the present study, we perform a 3-D tomography to a high quality 4-months data set described in Section 3.

3 Broadband data acquisition and processing

Our network comprised 2 CMG-40TD (0.016-50 Hz) Güralp and 5 CMG-ESP (0.008-50 Hz) broadband stations comprising 3-components seismometers (Figure 1). Data digitized with a sampling rate of 100 Hz was stored on local hard disks. The network recorded ground motions from the 25th of June till the 20th of October 2006. A detailled description of the broadband network, station set-up and data processing can be found in (Jousset and Francois, 2007). In addition, we used 3 stations from the permanent SIL network (Stefánsson et al., 1993; Jakobsdóttir, 2008), set to record continuously data during the 4 months of recording of the broadband network.

3.1 Earthquake detection, classification and catalogues

In order to detect events, we performed a Hilbert transform on each of the 3 components of the continuous data, and we computed the ratio between the STA (Short Term Average, 0.5 s) and LTA (Long Term Average, 10 s) of the velocity amplitude at each station. An event is detected when the STA/LTA ratio exceeds a threshold (fixed at 2 for our data set), for the three components at the same time.

If the threshold is too low, many events are detected, but may likely correspond to higher noise level; if the threshold is too high, low magnitude earthquakes may be missed, and the final data set is incomplete. If an event is detected at several stations of the network within a period of time compatible with the size of our network and reasonable average wave velocities within Hengill geothermal system, then one minute length data record (15 seconds before the trigger and 45 seconds after the trigger) are extracted for all stations.

By continuously tracking both the location of the stations and the number of stations that triggered the STA/LTA algorithm, we are able to give a first rough classification: large and close earthquakes will be recorded at all the stations, whereas small and localised earthquakes are recorded only at some of the station of the network. When an event is detected to at least 4 stations of our network, the waveform of the signal is extracted from the continuous data sorted and recorded into a directory according to the number of stations of the network that detected the event (data from all stations are extracted). Once event detection and automatic classification has been performed, a visual analysis of each waveform at each station is performed in order to read as much as information as possible from the data. This task consists in recording all valuable information seen in the waveforms that allows us to discriminate the waveform and identify the nature of the signal (noise, local earthquake, teleseism, LP event, ...), to locate earthquakes (P- and S- wave arrival times), to quantify the magnitude of the earthquakes, to quantify anisotropy in the area, ... These tasks have been automatized in "Seismotool", an integrated tool written in Matlab for network local seismicity analysis and processing (Jousset, 2006). our 4 months using sliding windows, as if data would be acquired in realtime.

This technique allowed us to detect more then 600 events from the 20th of June 2006 till the 19th of october 2006 and classify them. 500 micro-earthquakes (volcano-tectonic) located within the Hengill area, 40 tectonic earthquakes originating from outside Hengill volcano and 30 events comprising long periods, amongst which 10 are thought to be within Hengill area. Note that the SIL network recorded 130 locatable earthquakes for the same period of time, all detected by our detec-

tion algorithm. We conclude that our detection procedure was effective to catch smaller seismicity within Hengill volcano. The rate of seismicity is about more than 4 events a day (Figure 6) with periods of several earthquakes per minutes (for example 22nd of July). The detailed analysis of all event types is not performed in this work. In the present study, we focus on volcano-tectonic earthquakes, those having clear arrival times for P- and S- waves to perform the joint inversion for their hypocenter location and 3-D velocity model tomography.

3.2 P- and S- arrival times picking method

In order to pick the compressional (P) and shear (S) arrival times required for the tomography from the VT earthquakes, we implemented in "Seismotool" (Jousset, 2006) an algorithm consisting in computing An Information Criteria (Akaike, 1973) directely on the amplitude vector of the seismogram (Maeda, 1985), without using autoregressive coefficients, as in standard picking techniques (Leonard and Kennett, 1999). We did not used automatic phase-picker (Allen, 1982; Zhang et al., 2003) in order to have a better control on our data set and to apply the method also to the picking of S-wave, which are more difficult to be picked accurately, automatically. For a seismogram $x[1, N]$ of length N, the AIC value is defined as

$$\mathrm{AIC}(k) = k \log var(x[1, k]) + (N - k - 1) \log var(x[k + 1, N]) \qquad (1)$$

where k ranges through all the seismogram samples. When selecting windows where a wavelet is located, this AIC picker defines the onset point as the global minimum. For this reason, the time window must be chosen to include the segment of seismogram of interest only. For a very clear P-wave onset in the seismogram (Figure **??**), AIC values have a very clear AIC global minimum at the sample where the P-wave is thought to begin. For a low signal to noise ratio, the global minimum is not giving satisfactory results (Figure **??**). In addition, our broadband data includes also microseism which affect the AIC values, preventing accurate picking to be obtained, unless filtering is applied. In our data set, the best picking results are obtained when data are filtered int the range [1-30 Hz]. This picking

method minimizes errors due to change of operator and bias due to habit of a single operator after many picking. An estimation on picking error is also implemented in "Seismotool". The error is estimated by the use of two picking values instead of only one as usually done. The two picked times define a time interval during which the wave arrival time might be located with uniform probability. Figure 7 shows the statistics on P and S picks, revealing the quality of our data set.

4 Tomographic inversions

4.1 v_P/v_S ratio from the Wadati diagram analysis

A global first estimation of the mean v_P/v_S ratio can be determined by using the Wadati diagram in which the S-P interval time is plotted against the P-arrival time, t_P (Wadati, 1933). It can be used first to detect outliers in the picked arrival times and second as a priori information for tomographic inversions. We follow the approach of Chaterjee et al. (1985) in which the S-travel time is plotted against the P-travel time in order to estimate the v_P/v_S ratio from the data set. In this approach, the propagation time Δt_P of a P- wave in a medium of constant velocity v_P between an earthquake hypocenter eq happening at a time t_{eq} and the receiver R recording the wave at the arrival time t_p reads by definition $\delta t_P = d_P/v_P$, d_P being the distance of the path followed by the wave. The same applies for the S-wave. Assuming to the first order that the path of the P-wave and the path of the S-wave are the same, the ratio $r = v_P/v_S$ is defined as the ratio of the S-wave travel time to the P-wave travel time. Therefore, assuming a constant r ratio trhoughout the medium, picked P- and S- arrival times will align themselves along a straight line of slope r. Variations about the straight main line reflect velocity anomalies in the crust. In addition, once the ratio has been derived for an earthquake, it is possible to approximate the time of the earthquake as $t_{eq} = [1/(1-r)]\,(t_P - t_S)$.

The Wadati diagram allows us first to remove outliers, when points of the v_P and v_S are clearly outside the line defining the v_P/v_S ratio. These bad points

are certainly due to either bad $P-$ or $S-$ picks or both. For those points, either we removed then form the data set, or we checked to the seismograms to verify the picks. Errors were mainly due to errors on the $S-$ wave picks (about 25 cases) for remote stations (HEI and SAN), probably due to $S-$ to $P-$ wave conversions, and errors on the $P-$ pick, possibly due to too low amplitude signal/noise ratio.

After bad picks have been corrected, we applied the Wadati diagram analysis to our data set comprising 339 earthquakes. We find $v_P/v_S = 1.75 + / - 0.12$ as the global fit to all earthquakes picks (Figure 7). We also computed ratio for each earthquake separately, and averaged individual ratii. We find $v_P/v_S = 1.765 + / - 0.15$. These values are similar to the v_P/v_S ratio found from previous data analysis in Hengill area. Foulger (1995) and Miller et al. (1998) found $v_P/v_S = 1.77$ and Tryggvason et al. (2002) found $v_P/v_S = 1.78$).

4.2 Joint hypocenter location and 3-D model tomography inversion

We inverted our high quality data set comprising 339 earthquakes detected by at least 4 stations using model of increasing complexity. Many tomographic studies (Thurber, 1983; Eberhart-Phillips, 1990; 1993; Eberhart-Phillips and Michael, 1998), simultaneously invert local earthquake arrival times for hypocenters locations and 3-D velocity structure, in two steps: 1. joined inversion for 1-D velocity model and hypocenter locations; 2. joined inversion for 3-D velocity model and hypocenter locations. We performed an additional preliminary step, in order to increase the resolution of our model as shown below.

4.2.1 *a priori* hypocenter location for inversion and methodology

We performed two preliminary independent hypocenter location inversions using either a homogeneous model for P-waves of $5\,\mathrm{km\,s^{-1}}$ for inverting P-picks only and a homogeneous model for S-waves of $2.8\,\mathrm{km\,s^{-1}}$ for inverting S-picks only. The $P-$ and $S-$ velocity values used are average values taken from previous studies

at Hengill (Foulger, 1995; Miller et al., 1998; Tryggvason et al., 2002). These two inversions were implemented and performed in "Seismotool" (Jousset, 2006), by computing travel times at each station for sources located at regularly spaced nodes (500 meters) of 3-D grid spanning the whole area of Hengill volcano (15 km E-W $\times$ 15 km N-S $\times$ 10 km depth). Both grid searchs for P-wave travel times on the one hand and for S-wave travel times on the other hand, reveal that to the first order, earthquakes hypocenters locations fall in the area of our network. They display a similar distribution pattern of hypocenter locations in a plane perpendicular to the direction of the rift. For instance, results for the P-waves picked travel times are displayed in Figure **??**).

Using (or not) these *a priori* hypocenter locations, we then performed the two-step tomography approach applying the 1-D model inversion code VELEST (Ellworth et al., 1994) and the 3-D model inversion code SIMULSP12 (Thurber, 1993; Evans et al., 1994).

4.2.2 VELEST 1-D inversion

The first step consists in performing a joint inversion for hypocenter locations of the 339 detected earthquakes, 1-D velocity model and station corrections using VELEST (Kissling, 1994). Note that we may use the *a priori* hypocenter locations, or not. In the later case, we set all the hypocenters to an *a priori* depth of 4000 m and epicentres below the centre of the network, at the station HE3. For each case, we inverted for the v_P model using either P- or S- arrival times or both, and assuming a constant average $v_P/v_S = 1.76$ (based on the previous Wadati diagram analysis, see Figure 7), and using a wide range of starting velocity models, to estimate the resolution of the 1-D inverted model.

v_P 1-D model

We invert the P-wave velocity v_P model first, using both P-wave arrival times and S-wave arrival times. An initial test indicates that the use of P-wave arrival times only leads to improbable results (P-wave velocity not realistic). In

the case where we did not use the *a priori* hypocenter positions obtained from the grid search hypocenter determination, we ran two inversions with two different a priori hypocenter locations. *a priori* hypocenter locations have a strong influence on the inversion results, both in terms of the velocity model profile and value and hypocenter location at Hengill complex. Therefore, we used the *a priori* hypocenter locations from our preliminary grid-search inversion for all inversions. Figure 9 shows the final result of the 1-D inversion using *a priori* hypocenters obtained from the preliminary inversion using P- and S- arrival times. This P-wave velocity model is used as a priori information for inverting the v_P/v_S ratio. Note that throughout the inversions, each hypocenter is kept within 200 m.

Data variance from the inversion for the 1-D model is RMS=0.41349. Analysis of station corrections leads us to conclude that because these corrections are small (to the first order), the inverted hypocenters are rather accurate. In addition, stations corrections are systematically positive for the stations (HEI, KRO and SAN) located outside Hengill volcano, whereas station corrections within the network (HE1 to HE7) are all negative. This result may already point to 3-D structural features (Haberland et al., 2006).

v_P/v_S ratio 1-D model

The same approach is used to invert for the v_P/v_S ratio 1D model. Table 4 gives the final v_P velocity 1-D model used for the 3-D inversion, and results of the corresponding v_S velocity model and v_P/v_S ratio 1D model. It is hazardous to use the v_P/v_S ratio 1D model as such. Experience suggests that we should use the $v - P$ 1-D model as an initial model for the 3-D inversion and not for any preliminary interpretation. Note however, that a low v_P/v_S ratio anomaly results from the inversion at shallow depth, which is consistent with Tryggvason et al. (2002)'s conclusion of the existence of a low v_P/v_S ratio below Hengill volcano.

4.3 3-D inversion using SIMULPS12

We performed 3-D tomography using SIMULSP12 (Evans et al., 1994). As pointed out by Evans et al. (1994), we first filtered out all earthquakes for which the epicentre location makes an angle with any couple of two stations greater than 180 degrees. The number of earthquakes in the reduced data set drops down to 269 earthquakes. We used the 1-D v_P model and we varied v_P/v_S values as starting models in subsequent inversions. The structure is parameterized by the values of the P-wave velocity v_P and the v_P/v_S ratio at the nodes of a 3-D grid, and the observed P- and S- arrival times are inverted by an iterative least-squares method to determine simultaneously the coordinates of earthquakes hypocentres and the values of v_P and v_P/v_S ratio at the grid nodes. Tri-linear interpolation is used between nodes for v_P and the v_P/v_S ratio between the nodes. The ray paths are calculated with an approximate 3-D ray tracing algorithm that produces curved, non planar ray paths, which are defined by points more finely spaced than the velocity grid. The solution is obtained by iterative damped least squares inversion. For each iteration, new ray paths are determined, the hypocenter solution is included, and parameter separation is performed. Weighting is applied to each observation based on the size of the travel time residual and source-receiver distance. The full resolution matrix is calculated (Yao et al., 1999).

4.3.1 Trade-off curve

A damping parameter is used to stabilize the inversion (Eberhart-Phillips, 1986; Haberland et al., 2006). If the damping parameter is not used (no damping), the inversion produces instabilities leading to spatial oscillations of the velocity, but they do not correspond to any geophysical significance. In order to avoid such oscillations, an increased damping value is used. If the damping is too large, then velocity variations are minimized in the model and the 1D velocity model is kept, with larger data variance (up to a maximum corresponding to the data variance with the 1-D velocity model). There is a trade-off between data variance and model variance to be found. The optimal value of the damping is the one for which the

data variance is minimum with acceptable model variance. The model variance corresponds to the 3D anomalies with respect to the 1D model. To summarize, prior to each 3-D inversion, the damping parameter is chosen empirically by evaluating a trade-off curve of data variance and solution variance as the damping varies with the model grid and the data set (Eberhart-Phillips, 1986; Haberland et al., 2006). Figure 10 shows an example of the trade-off curve of the damping parameter computed for a grid sampling of 2 km in the case of P-wave velocity 3-D model inversion.

4.3.2 v_P 3-D inversion

We performed a series of simultaneous hypocenter-velocity inversions progressively increasing the complexity in the model. This strategy proved to be successful, as the data variance decreased after each step. We also refined the mesh of the 3-D grid. We started using a coarse 3-D grid spacing of 2 km, with several nodes outside the target geothermal system, in order to constrain the volume that our data set can image. This first model has a RMS=0.04874. In a second inversion process, we refined the grid to 1-km grid spacing, in order to test the ability of our data set to image more accurately the geothermal system without to great loss of resolution (Figure 17 and Figure 18). This second model has a RMS=0.06630. Comparisons between the inversion results and resolution analysis for inversion grid spacing show that a grid spacing of 1 km is a spacing that produces excellent image fidelity without serious loss of resolution for the critical region directly below our network. A more complete analysis would be to decrease smoothly the grid spacing and compare the loss of model resolution and variance. Results are shown on 2 cross-sections (NS and EW) and horizontal slices at different depths (Figure 11). The same iterative approach has been used to invert for the v_P/v_S ratio and earthquake hypocenters (Figure 12).

After the last 3-D inversion has been performed, we further improved earthquakes hypocenters by using a double-difference technique (Slunga et al., 1995; Waldhauser and Elsworth, 2000). Finally, using the relocated earthquake posi-

tions and starting from the best 3-D velocity model, we performed an ultimate 3-D inversion to adjust the final velocity model and final hypocenter positions.

4.4 Resolution and robustness of models

Christian and Klaus can you check and complete here please?

The resolution matrix describes the distribution of information for each node, such that each row is the averaging vector for a parameter Eberhart-Phillips and Michael (1998). Estimating model fidelity or resolution in earthquake tomography may be performed by several means, e.g., inspecting the diagonal elements of the resolution matrix (Roeker, 1982), or by evaluating reconstructed synthetic models (e.g., checkerboards) for the specific geometry (Hunphreys and Clayton, 1988; Eberhart-Phillips and Michael, 1998)

Klaus: do we need a checker-board to be performed and explained here?

5 Discussion and conclusions

5.1 Seismic tomography

Within the framework of two European projects (IGET and ENGINE), a joined study between BRGM, GFZ and ISOR has been performed in order to improve our knowledge of the Hengill geothermal system. A network of 7 broadband seismometers from BRGM and GFZ instrumental pools have been installed and the analysis of 4 months continuous data was performed together with data from the Icelandic SIL network.

Data analysis of the data allowed us to record about 500 micro-earthquakes (volcano-tectonic) located within the Hengill area, 40 tectonic earthquakes originating from outside Hengill volcano and 30 events with long periods, amongst which 10 LP earthquakes were located within the Hengill area. Owing the emergent characteristics, of the LP signals, their accurate location and source mecha-

nism determination cannot be based on the P- and S- wave travel time inversion, and requires accurate velocity models to be known.

The understanding of the complex structure of the geothermal system beneath Hengill volcano and its relationship with seismicity requires independent estimates of both P- and S- velocity variations, and of vP/vS ratio. We used tomography techniques (e.g. Haberland et al., 2006) to improve the resolution of the 3-D velocity model structure of Hengill geothermal system. Results reveal a high v_P anomaly body in Olkelduhals area at a depth of about 3 to 5 km and a low v_P/v_S ratio below Hengill volcano. Our results confirm previous observations from Foulger (1995), with additional new details and an increased resolution. The number of stations used for our tomography is certainly too small to get more accurate details of the geothermal field. It has been however shown that the location of the stations is more important than the number of stations to image the same structure. It is better to have properly chosen useful stations rather than having many stations badly located. As a test, in order to estimate the effect of the number of stations, we performed one inversion using the same network, and removing station HE5. The result of the best inversion reveals that the main features of the inverted structure are still visible. Hypocenter locations are much less clustered in the northern area (close to Nesjavellir), but not in the main cluster of seismicity.

5.2 Detailled structure of Hengill geothermal system

Other geophysical techniques have been applied to the Hengill high-temperature area citepbjornsson1986. For instance, a resistivity map was obtained (Gunnarsson et al., 1992). Within the IGET project, other observations like Transient Electromagnetism surveys and 3D magneto-telluric profiles have been performed all over the area (Arnórsson et al., 2008). The inversion of MT data reveals a low resistivity cylindrical body below Okelduhals at depths ranging 2.5-5 km. This corresponds to the location of the high P-wave velocity body inverted here, and is very close to the inflation source location observed in 1995 (Feigl et al., 2000) and interpreted as a magma intrusion.

5.3 Reservoir modelling: supercritical fluids?

This promising results suggests that et up a model in which 3D wave propagation is triggered and compare with data. required parameters (given by previous data analysis or assumption) P, T, gaz composition, liquid/gas ratio, how many fractures? test to be confirmed with several fractures size and shape and location of fractures?

Tryggvason et al. (2002) report clusters of deep earthquake to occur below the brittle layer. We did not observe such deep earthquakes during our experiment. This suggests that the strain rate was normal during the 4 months of our experiment.

An analysis of the source mechanisms would allow to relate the stress pattern in the area and reflect the structural features shown here (really? to what extent, how?)

Towards a permanent network for monitoring geothermal field: The 3-D velocity model obtained will be useful in deciding the most valuable locations to site additional instrumentation.

Acknowledgements

This study was funded by FP6 European Community IGET (contract 518378) and ENGINE (contract 019760). 5 broadband instruments are from GFZ instrumental pool, and two belong to BRGM. We would like to thank E.A. Gudnason, G. S. Hilmarsson, H. O. Stefánsson, J. E. Jńsson, S. A. Hálldorsson, Th. Agústsdottir and Th. Björnsdóttir for their valuable help during the field work. Many thanks to Michael Weber and Hubert Fabriol for many valuable discussions and advises.

References

Akaike, H. (1973). Information theory and an extension of the maximum likelihood principle. In *Budapest Akademiai Kiado*, pages 267–181. B. Petrov and F. Csaki (Editors).

Allen, R. V. (1982). Automatic phase pickers: their present use and future prospects. *Bull. Seismol. Soc. Am.*, 72:S225–242.

Arnórsson, S., Axelsson, G., and Saemundsson, K. (2008). Geothermal systems in Iceland. *Jökull*, 58:269–302.

Barnea, J. (1972). United Nations approach and accomplishments in the field of geothermal resources development. *Geothermics*, 1:164–167.

Benz, H. M., Chouet, B. A., Dawson, P. B., Lahr, J. C., Page, R. A., and Hole, J. A. (1996). Three-dimensional P and S wave velocity structure of Redoubt volcano, Alaska. *J. Geophys. Res.*, 101(B4):8111–8128.

Bödvarsson, G. (1970). An estimate of the natural heat resources in a thermal area in Iceland. *Geothermics*, 2:1289–1293.

Brenguier, F., Shapiro, N. M., Campillo, M., Nercessian, A., and Ferrazzini, V. (2007). 3-D surface wave tomography of the Piton de la Fournaise volcano using seismic noise correlations. *Geophys. Res. Lett.*, page L02305.

Chaterjee, S., Pitt, A., and Iyer, H. (1985). v_p/v_s ratios in the Yellowstone National Park Region, Wyoming. *J. Volcanol. Geotherm. Res.*, 26:213–230.

Chouet, B. (1996). *New methods and future trends in seismological volcano monitoring.*, pages 23–97. Scarpa/Tilling, Springer-Verlag, Berlin Heidelberg.

Dangel, S., Schaepman, M., Stoll, E., Carniel, R., Barzandji, O., Rode, E., and Singer, J. (2003). Phenomenology of tremor-like signals observed over hydrocarbon reservoirs. *J. Volcanol. Geotherm. Res.*, 128:135–158.

Eberhart-Phillips, D. (1986). Three-dimensional velocity structure in the northern California coast ranges from inversion of local earthquake arrival times. *Bull. Seismol. Soc. Am.*, 76:1025–1052.

Eberhart-Phillips, D. (1990). Three-dimensional P and S velocity structure in the Coalinga region, California. *J. Geophys. Res.*, 95:15343–15363.

Eberhart-Phillips, D. (1993). *Local earthquake tomography: earthquake source region*, pages 613–643. Eds Iyer, H.M and Hihara K. and Chapman & Hall, London.

Eberhart-Phillips, D. and Michael, A. J. (1998). Seismotectonics of the Loma Prieta, California, region determined from three-dimensional V_P, V_P/V_S, and seismicity. *J. Geotherm. Res*, 103(B9):21099–21120.

Ellworth, E. K. W., Eberhart-Phillips, D., and Kradolfer, U. (1994). Initial reference models in local earthquake tomography. *J. Geophys. Res.*, 99:19635–19646.

Ellworth, W. L., Eberhart-Phillips, D., and Kissling, E. (1991). A test of local earthquake tomography. *Seism. Res. Lett.*, 62:31.

Evans, J. R., Eberthart-Phillips, D., and Thurber, C. H. (1994). User's manual for $SIMULPS12$ for imaging v_p and v_p/v_s: a derivative of the "thurber" tomographic inversion $SIMUL3$ for local earthquakes and explosions. *USGS - Open-file report*, 94-431:1–101.

Evans, J. R., Foulger, G. R., Julian, B. R., and Miller, A. (1996). Crustal shear-wave splitting from the local earthquakes in the Hengill triple junction, southwest Iceland. *Geophys. Res. Lett.*, 23(5):455–458.

Feigl, K., Gasperi, G., Sigmundsson, F., and Rigo, A. (2000). Crustal deformation near Hengill volcano, Iceland 1993-1998: coupling between magmatic activity and faulting inferred from elastic modelling of satellite radar interferrograms. *J. Geophys. Res.*, 105:25655–25670.

Foulger, G. R. (1988a). The Hengill triple junction, SW Iceland: 1. tectonic structure and the spatial and temporal distribution of local earthquakes. *J. Geophys. Res.*, 93:13493–13506.

Foulger, G. R. (1988b). The Hengill triple junction, SW Iceland: 2. anomalous earthquake focal mechanisms and implications for process within the geothermal reservoir and at accretionary plate boundaries. *J. Geophys. Res.*, 93:13507–13523.

Foulger, G. R. (1995). The Hengill geothermal area, Iceland: variation of temperature gradients deduced from the maximum depth of seismogenesis. *J. Volcanol. Geotherm. Res.*, 65:119–133.

Foulger, G. R. and Long, R. (1984). Anomalous focal mechanism solutions: evidence for tensile crack formation on an accretionary plate boundaries. *Nature*, 310:43–45.

Foulger, G. R., Long, R., P., E., and Björnsson, A. (1989). Implosive earthquakes at the active accretionary plate boundary in Iceland. *Nature*, 337:640–642.

Foulger, G. R., Miller, A., Julian, B., and Evans, J. (1995). Three-dimensional v_p and v_p/v_s structure of the Hengill Triple Junction and geothermal area, Iceland, and the repeatability of tomographic inversion. *Geophys. Res. Lett.*, 22(10):1309–1312.

Foulger, G. R. and Toomey, D. (1989). Structure and evolution of the Hengill-Grendalur central volcano complex, Iceland: geology, geophysics and seismic tomography. *J. Geophys. Res.*, 94:17511–17522.

Golub, G. H. and Reinsch, C. (1971). *Singular value decomposition and least squares solutions*, pages 134–151. J.H. Wilkinson and C. Reinsch, Springer-Verlag, New-York.

Gunnarsson, A., Steingrimsson, B., Gunnlaugsson, E., Magnusson, J., and Maack, R. (1992). Nessjavellir geothermal co-generation power plant. *Geothermics*, 21(4):559–583.

Haberland, C., Rietbrock, A., Lange, D., Bataille, K., and Hofmann, S. (2006). Interaction between forearc and oceanic plate at the south-central Chilean margin as seen in local seismic data. *Geophys. Res. Lett.*, 33:L23302.

Hunphreys, E. and Clayton, R. W. (1988). Adaptation of back projection tomography to seismic travel time problems. *J. Geophys. Res.*, 93:4731–4735.

Ingolfsson, O., Sigmarsson, O., Sigmundsson, F., and Símonarson, L. (2008). The dynamic geology of Iceland. *Jökull*, 58:1–2.

Iyer, H. M. and Hirahara, K. (1993). *Seismic Tomography: Theory and practice*. Chapman and Hall, London, UK.

Jakobsdóttir, S. (2008). Seismicity in Iceland. *Jökull*, 58:75–100.

Jousset, P. (2006). Sismologie large bande: méthodologie et applications: apport en géothermie haute enthalpie à Bouillante, Guadeloupe. *Rapport BRGM RP-54701-FR*, page 119 pp.

Jousset, P. and Francois, B. (2007). Set-up of a broadband seismological network at Hengill geothermal field (Iceland). *Rapport BRGM*, RP-54971-FR:1–51.

Julian, B. R., Miller, A., and Foulger, G. R. (1997). Non-double couple earthquake mechanisms at the Hengill-Grensdalur volcanic complex. *Geophys. Res. Lett.*, 24(7):743–746.

Kissling, E. (1988). Geotomography with local earthquake data. *Rev. Geophys*, 26:659–698.

Koulakov, I., Bohm, M., Asch, G., Luehr, B.-G., Manzanares, A., Brotopuspito, K. S., Fauzi, P., Purbawinata, M. A., Puspito, N. T., Ratdomopurbo, A., Kopp, H., Rabbel, W., and Shevkunova, E. (2007). P and S velocity structure of the crust and the upper mantle beneath central Java from local tomography inversion. *J. Geophys. Res.*, 112(B08310).

Lees, J. M. and Crosson, R. S. (1989). Tomographic inversion for three-dimensional velocity structure at Mount St. Helens using earthquake data. *J. Geophys. Res.*, 94:5716–5728.

Leonard, M. and Kennett, B. (1999). Multi-component autoregressive techniques for the analysis of seismograms. *Phys. Earth. Planet. Interiors*, 113:247–264.

Lokmer, I., Bean, C., Saccorotti, G., and Patanè, D. (2007). Moment-tensor inversion of LP events recorded on Etna in 2004 using constraints obtained from wave simulation tests. *Geophys. Res. Lett.*, 34(22):L22316.

Maeda, N. (1985). A method for reading and checking phase times in auto-processing system of seismic wave data. *Zizin=Jishin*, 38:365–379.

Michelini, A. (1993). Testing the reliability of V_P/V_S anomalies in travel time tomography. *Geophys. J. Int.*, 114:405–410.

Miller, A., Julian, B., and Foulger, G. R. (1998). Three-dimensional seismic structure and moment tensors of non-double couple earthquakes at the Hengill-Grensdalur volcanic complex, Iceland. *Geophys. J. Int.*, 133:309–325.

Neuberg, J., Luckett, R., Ripepe, M., and Braun, T. (1994). Highlights from a seismic broadband array on Stromboli volcano. *Geophys. Res. Lett.*, 21(9):749–752.

Norris, A. (1985). A differential scheme for the effective moduli of composites. *Mech. Mater.*, 4:116.

Pavlis, G. L. and Booker, J. R. (1980). The mixed discrete-continuous inverse problem: application to the simultaneous determination of earthquake hypocentres and velocity structure. *J. Geophys. Res.*, 85:4801–4810.

Pedersen, R., Sigmundsson, F., and Einarsson, P. (2007). Controlling factors on earthquake swarms associated with magmatic intrusions; contraints from Iceland. *J. Volcanol. Geotherm. Res.*, 162:73–80.

Roeker, S. W. (1982). Velocity structure of the Pamir-Hindu Kush region: possible evidence of subducted crust. *J. Geophys. Res.*, 87:945–959.

Rögnvaldsson, S., Gudmundsson, A., Agustsson, K., Jakobsdóttir, S., Slunga, R., and Stefánsson, R. (1998). *Overview of the 1993-1996 seismicity near Hengill*, pages volume VI–R98006–JA05. Vedustofa Islands, Reykjavik.

Saemundsson, K. (1995). *Hengill, Jardhiti, Ummyndun og Grunnvatn, 1:25000 (Hengill, Geothermal, Alteration and Groundwater).* Orkustofunun.

Sens-Schönfelder, C., Korn, M., and Stefánsson, R. (2006). Joint interpretation of the size and time distributions of seismic activity around the Hengill triple junction (SW Iceland) between 1993 and 1996. *J. Seismol.*, B7:15151–15161.

Sigmundsson, F., Einarsson, P., Rögnvaldsson, S. T., Foulger, G. R., Hodgkinson, K. M., and Thorbergsson, G. (1997). The 1994-1995 seismicity and deformation at the hengill triple junction, Iceland: triggering of earthquakes by minor magma injection in a zone of horizontal shear stress. *J. Geophys. Res.*, 102(B7):15151–15161.

Slunga, R., Rognvaldsson, S. T., and Bodvarsson, R. (1995). Absolute and relative locations of similar events with application to microearthquakes in southern Iceland. *Geophys. J. Int.*, 123:409–419.

Spencer, C. and Gubbins, D. (1980). Travel-time inversion for simultaneous earthquake location and velocity structure determination in laterally varying media. *geophys. J. R. Astron. Soc.*, 63:95–116.

Stefánsson, R., Bödvarsson, R., Slunga, R., Einarsson, P., Jakobsdóttir, S., Bungum, H., Gregersen, S., Havskov, J., Hjelme, J., and Korhonen, H. (1993). Earthquake prediction research in the South Iceland Seismic Zone and the SIL Project. *Bull. Seismol. Soc. Am.*, 83:696–716.

Thurber, C. H. (1983). Earthquake locations and three-dimensional crustal structure in the Coyote Lake area, central California. *J. Geophys. Res.*, 88(B10):8226–8236.

Thurber, C. H. (1986). Analysis methods for kinematic data from local earthquakes. *Rev. Geophys.*, 24:793–805.

Thurber, C. H. (1993). *Local earthquake tomography: velocities and V_P/V_S-theory*, pages 563–583. Eds Iyer, H.M and Hihara K. and Chapman and Hall, London.

Toomey, D. R. and Foulger, G. R. (1989). Application of tomographic inversion to local earthquake data from the Hengill-Grendalur central volcano complex, Iceland. *Phys. Earth and Plan. Int.*, 94:17497–17510.

Tryggvason, A., Rögnvaldsson, S. T., and Flovenz, O. G. (2002). Three-dimensional imaging of the P and S-wave velocity structure and earthquake locations beneath Southwest Iceland. *Geophys. J. Int.*, 151:848–866.

Waldhauser, F. and Elsworth, W. (2000). A double-difference earthquake location algorithm: method and application to the Northern Hayward fault, California. *Bull. Seism. Soc. Am.*, 90(6):1353–1368.

Ward, P. L. (1972). Microearthquakes: prospecting tool and possible hazard in the development of geothermal resources. *Geothermics*, 1:3–12.

Yao, Z. S., Roberts, R. G., and Tryggvason, A. (1999). Calculating resolution and covariance matrices for seismic tomography with the LSQR method. *Geophys. J. Int.*, 138:886–894.

Zhang, H., Thurber, C., and Rowe, C. (2003). Automatic P-wave arrival detection and picking with multiscale wavelet analysis for single-component recordings. *Bull. Seismol. Soc. Am.*, 93(5):1904–1912.

A Tomographic inversion method

A.1 Basic theory

The arrival time of a seismic wave from an earthquake at a station is a non-linear function of the earthquake location, which includes its spatial coordinates (x_1, x_2, x_3) and earthquake origin time τ, and the velocity structure along the wave path. According to the ray theory, this nonlinear functional relationship can be written as

$$t = \tau + \int_{l[u(r)]} u(r) dl \tag{2}$$

where t is the arrival time, $u(r)$ is the slowness or reciprocal of velocity, dl is the differential length along the ray, and $l[u(r)]$ i the ray path, a function of the earthquake hypocenter and velocity structure along the ray path. For a pair (earthquake (i), receiver (j)), linearisation of equation 2 about a starting model and earthquake location results in the equation

$$r_{ij} = \sum_{k=1}^{3} \frac{\partial T_{ij}}{\partial x_k} \Delta x_k + \Delta \tau_i + \int_{\text{raypath}} \delta u(r) dl \tag{3}$$

where r_{ij} is the arrival time residual, T_{ij} is the travel time from the i^{th} earthquake to the j^{th} station, $\partial T_{ij}/\partial x_k$ are the partial derivatives of travel time with respect to the spatial coordinates, Δx_k and $\Delta \tau_i$ are perturbations to the starting earthquake hypocenter, and $\delta u(r)$ is the slowness perturbation to the reference model. The arrival time residual is the difference between the observed arrival time and the theoretical arrival based on the starting earthquake location and the reference velocity model.

A.2 Parametrization of the structure

The parametrization of the structural reference model may take several forms Thurber (1993). The most used way is to use a uniform or non uniform grid of constant slowness cells (e.g., Benz et al., 1996). Other ways have been introduced

Koulakov et al. (2007).

When the reference model is parametrized as a uniform grid of constant slowness cells, the system of equations may be written in a matrix form (Tryggvason et al., 2002)

$$\begin{bmatrix} \gamma_i^P \\ \gamma_i^S \end{bmatrix} = \begin{bmatrix} A_i^P & B_i^P & 0 \\ A_i^S & 0 & B_i^S \end{bmatrix} \begin{bmatrix} \Delta h_i \\ \Delta u^P \\ \Delta u^S \end{bmatrix} \tag{4}$$

where A_i is the matrix of partial derivatives of traveltimes with respect to hypocentre location, Δh_i is the vector of hypocentre perturbations, B_i is the matrix of distances travelled in each cell and Δu the vector of slowness perturbations. Superscript P and S are for the $P-$ and $S-$ wave respectively. The coupling between the $P-$ and $S-$ velocity models and the hypocentre locations is in this equation very clear.

A.3 Inversion

Accurate determination of the velocity structure requires a large number of sources, resulting in a huge number of unknowns. Whereas direct inversion via Singular Value Decomposition would be the best approach (Thurber, 1993), the solution of this system of equations makes use of the property

$$\boldsymbol{U_0^T A_i = 0} \tag{5}$$

where U_0 are the eigenvectors associatied with the zero singular values of $A_i\, A_i^T$ (Golub and Reinsch, 1971). This property allows the separation between slowness and hypocenter perturbations (Pavlis and Booker, 1980; Spencer and Gubbins, 1980).

Model parametrization artifacts and solution instability may also be minimized using constraint equations (Lees and Crosson, 1989; Benz et al., 1996; Tryggvason et al., 2002).

A.4 Resolution

The resolution matrix computed in the simultaneous inversion of hypocenters and velocity (Thurber, 1993) provides necessary information for interpretation regarding the distribution of ray-paths and the degree and pattern of smoothing. Michelini (1993) compute the resolving width, S_j, for a grid point from all the elements, s_{ij} of the corresponding row of the resolution matrix, weighted by their distance, D_{ij}, from the grid point,

$$S_j = \log \left[|s_j|^{-1} \sum_{k=1}^{N} \left(\frac{s_{kj}}{|s_j|} \right)^2 D_{jk} \right]. \tag{6}$$

The spread has also been introduced to indicate how widely the wave speed is averaged to yield the model values.

$$\text{spread} = \left[\|\mathrm{R_j}\|^{-2} \sum_{\mathrm{k}} \mathrm{D_{jk}^2 R_{jk}^2} \right]^{1/2} \tag{7}$$

where R_{jk} is an element of the resolution matrix, $\|R_j\|$ is the Euclidean (L2) norm of its j^th row, and D_{jk}^2 is the distance between the j^{th} and the k^{th} nodes.

TABLES:

Table 1:

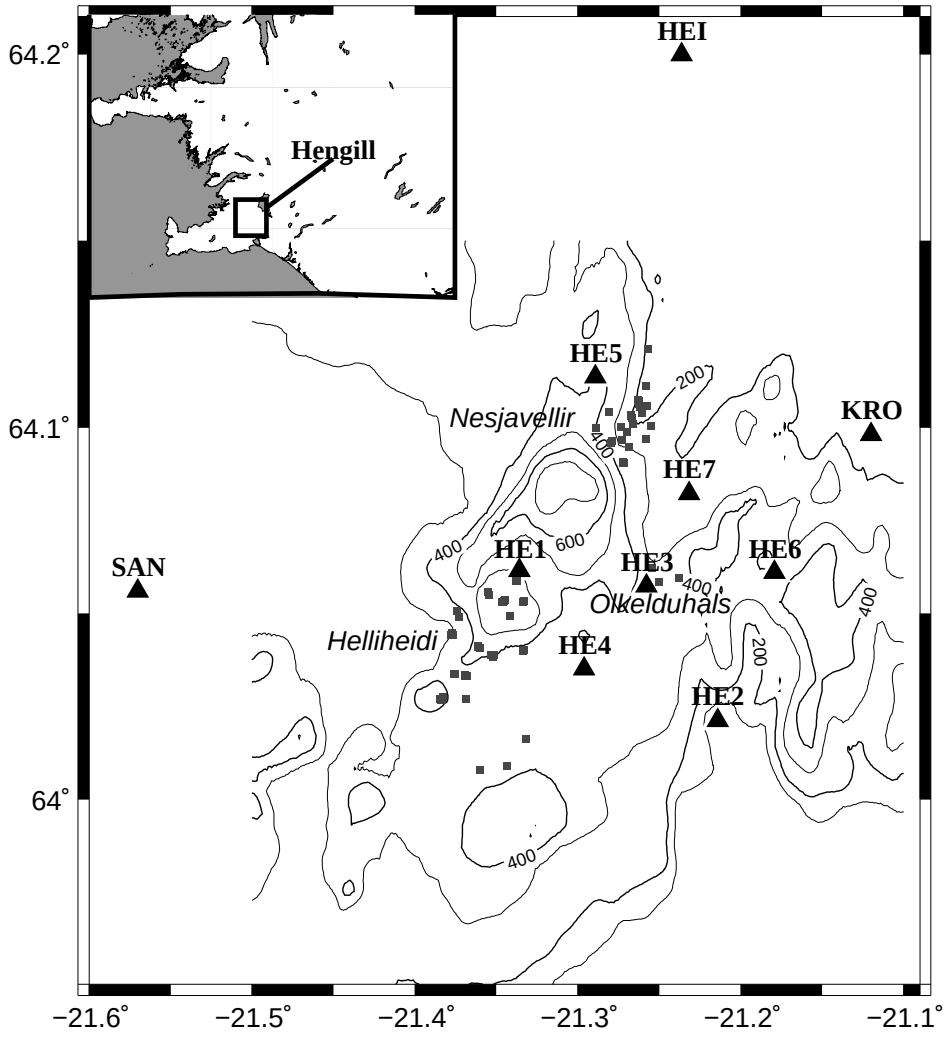

Figure 1: Topographic map of Hengill Volcano, Iceland, with the location of the broadband seismological stations (HE1, HE2, HE3, HE4, HE5, HE6, HE7) and SIL network stations (KRO, SAN, HEI). Small grey squares are locations of geothermal wells; they are grouped in three areas (Nesjavellir, Helliheidi and Olkelduháls). Inlet shows the location of Hengill volcano in Iceland.

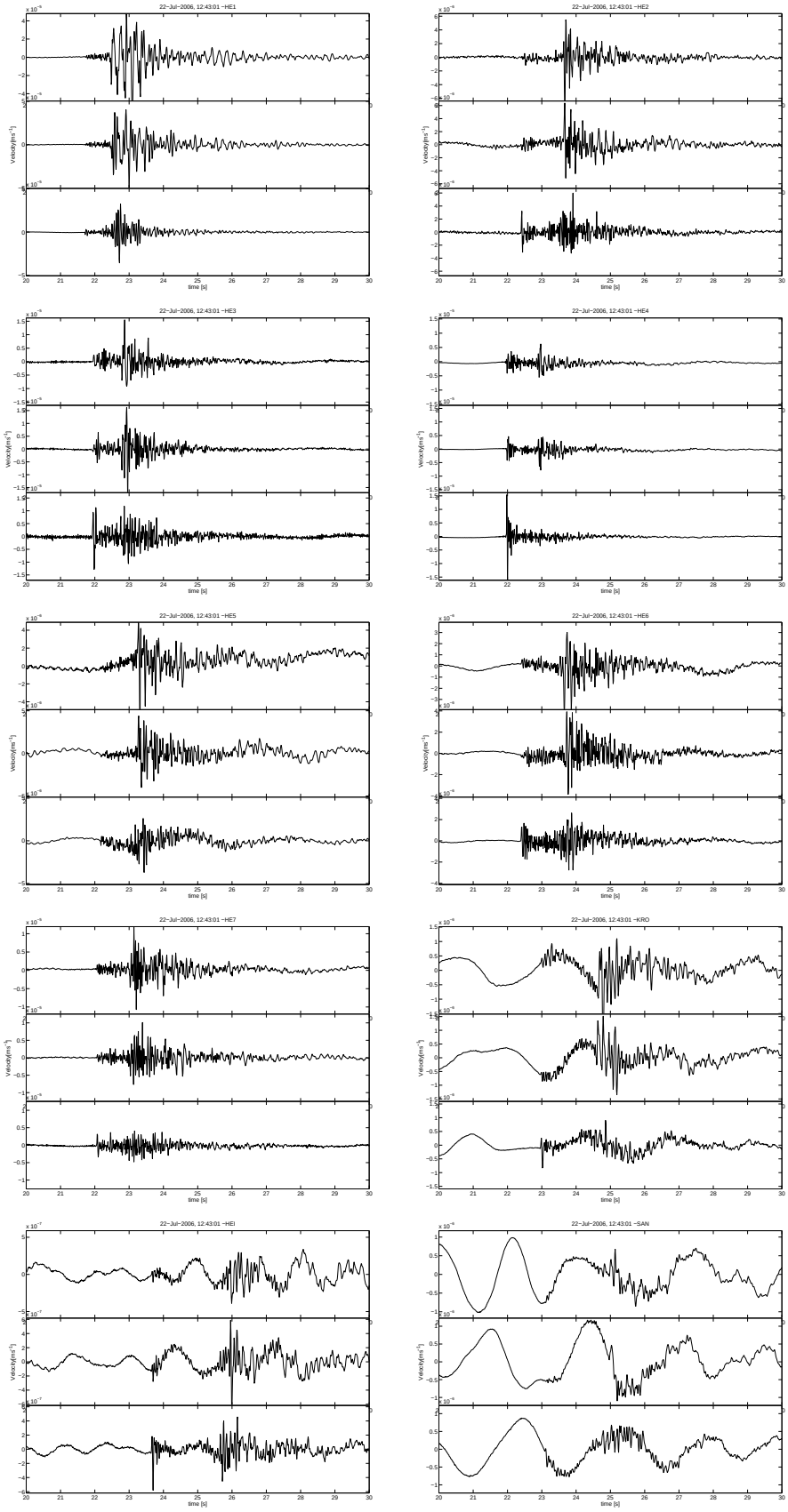

Figure 2: Example of a volcano-tectonic earthquake (July, 22^{nd}, 2006, 12:43) recorded at the IGET Hengill seismic network and used for the tomographic inversion. Unfiltered data.

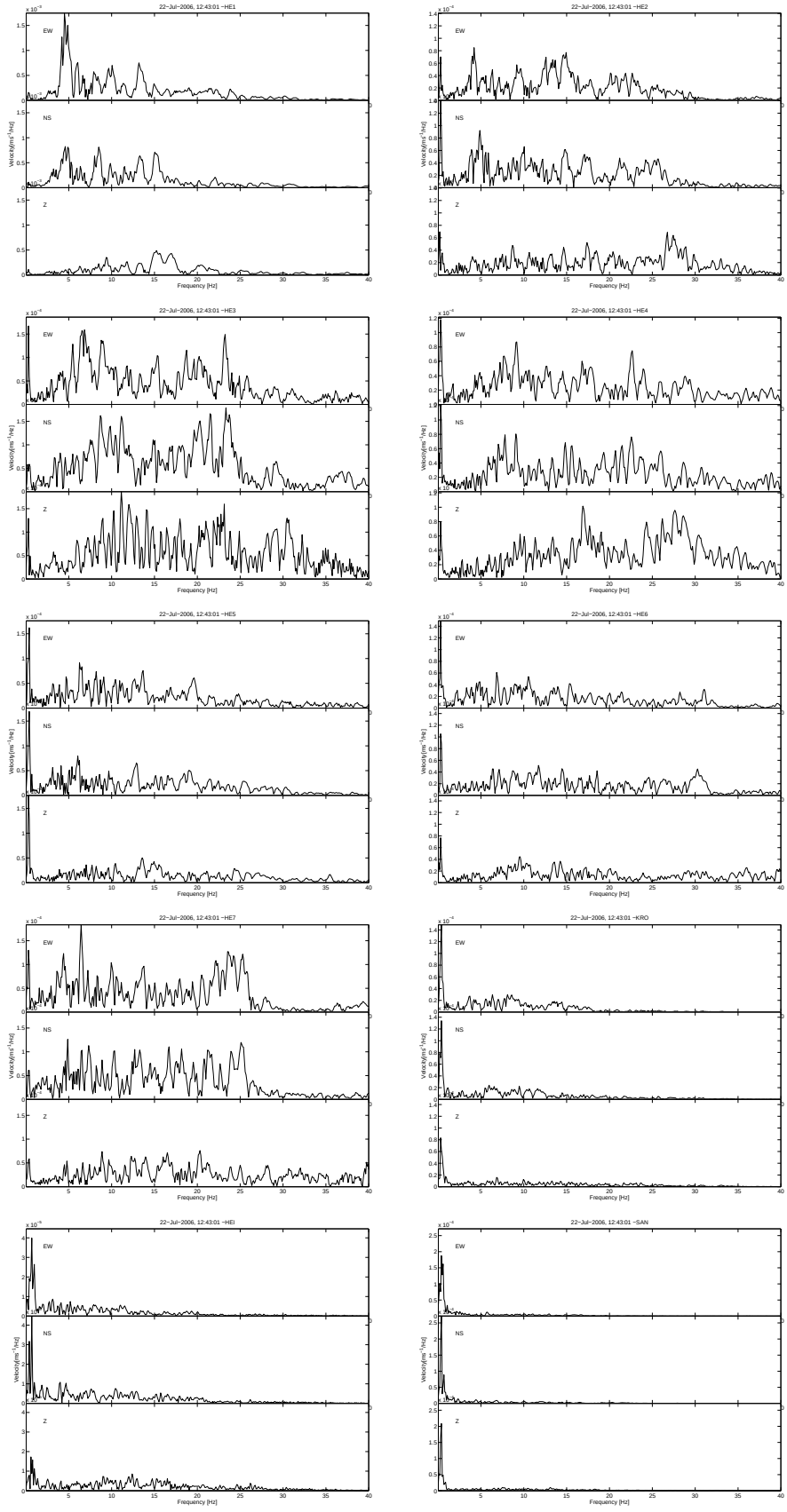

Figure 3: Spectra of the earthquake shown in Figure 2

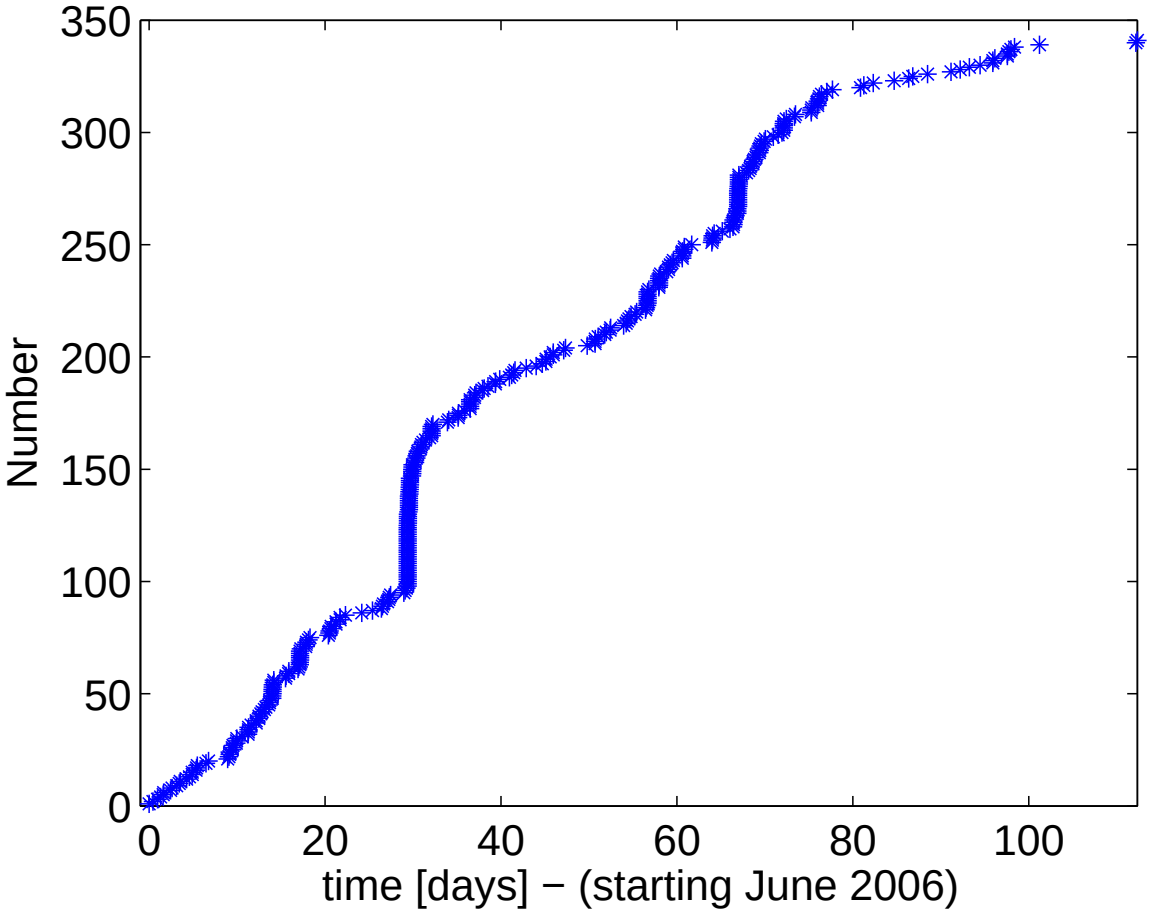

Figure 4: Cumulative number of earthquakes recorded at IGET Hengill seismic network between June 26th, 2006 till October 17th, 2006.

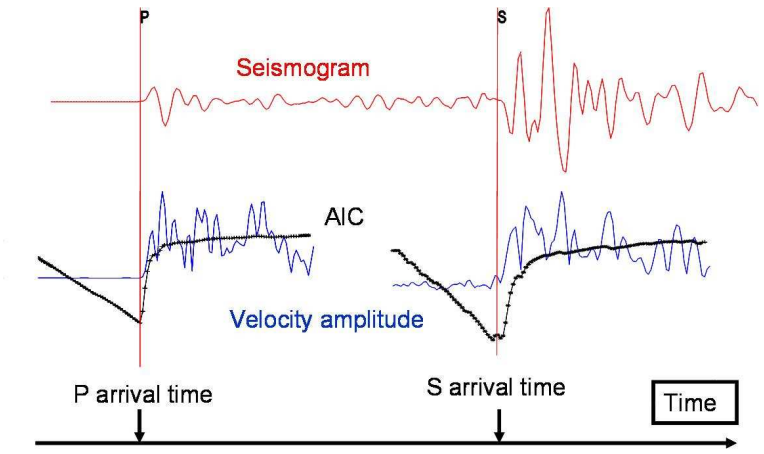

Figure 5: Example of the picking technique using AIC criteria.

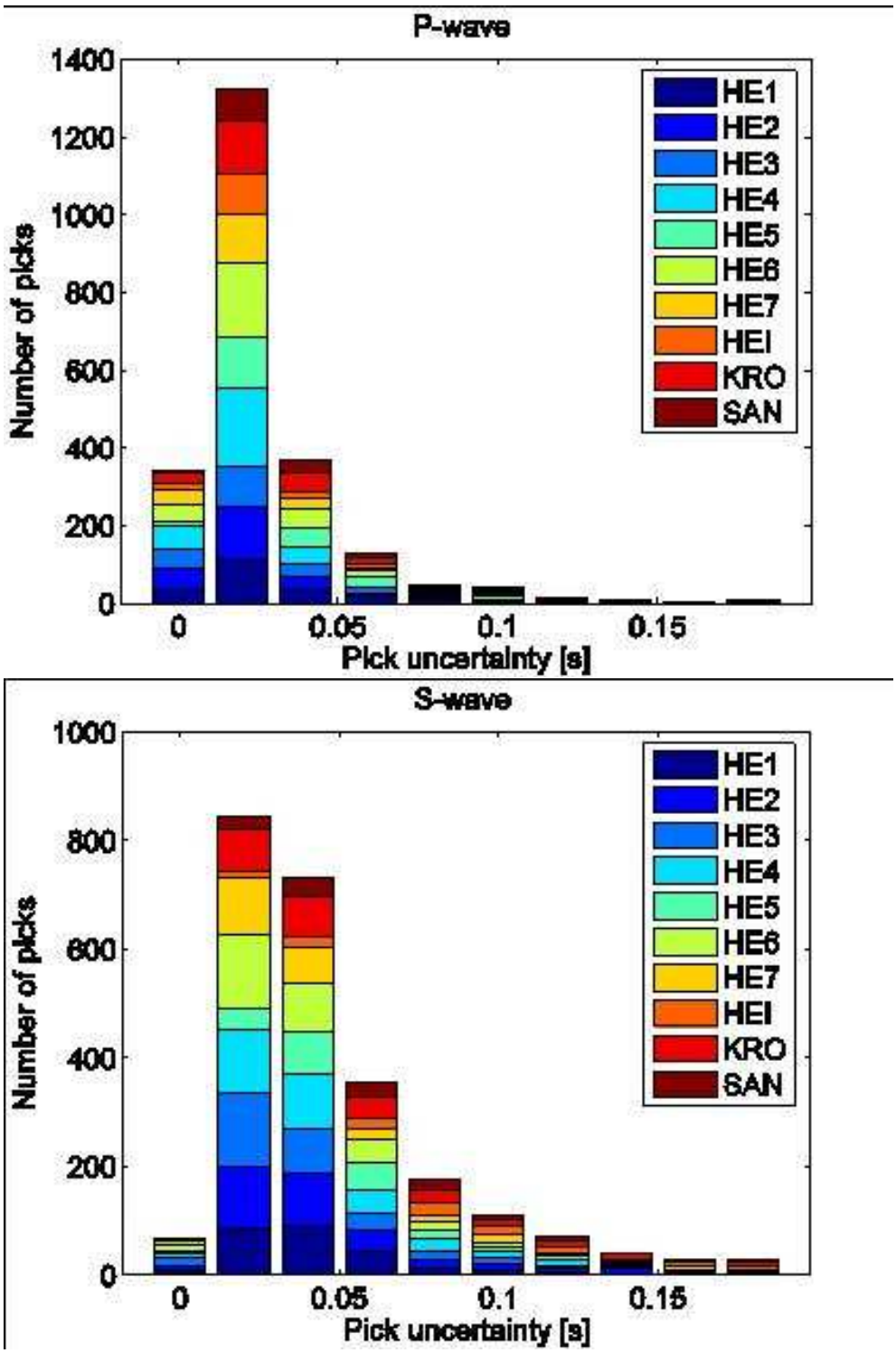

Figure 6: Statistics of the (top) P-wave and (bottom) S-wave arrival times picking for the 343 VT earthquake recorded at IGET seismic network.

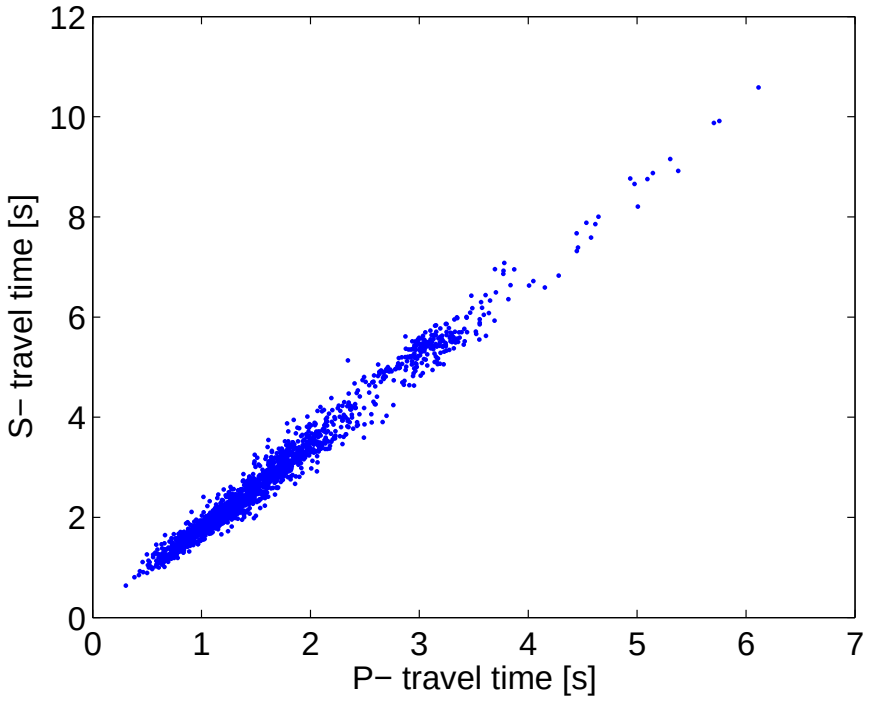

Figure 7: Wadati diagram for 240 VT earthquakes recorded at Hengill with the IGET seismic network. The slope is $v_P/v_S = 1.765 + / - 0.12$.

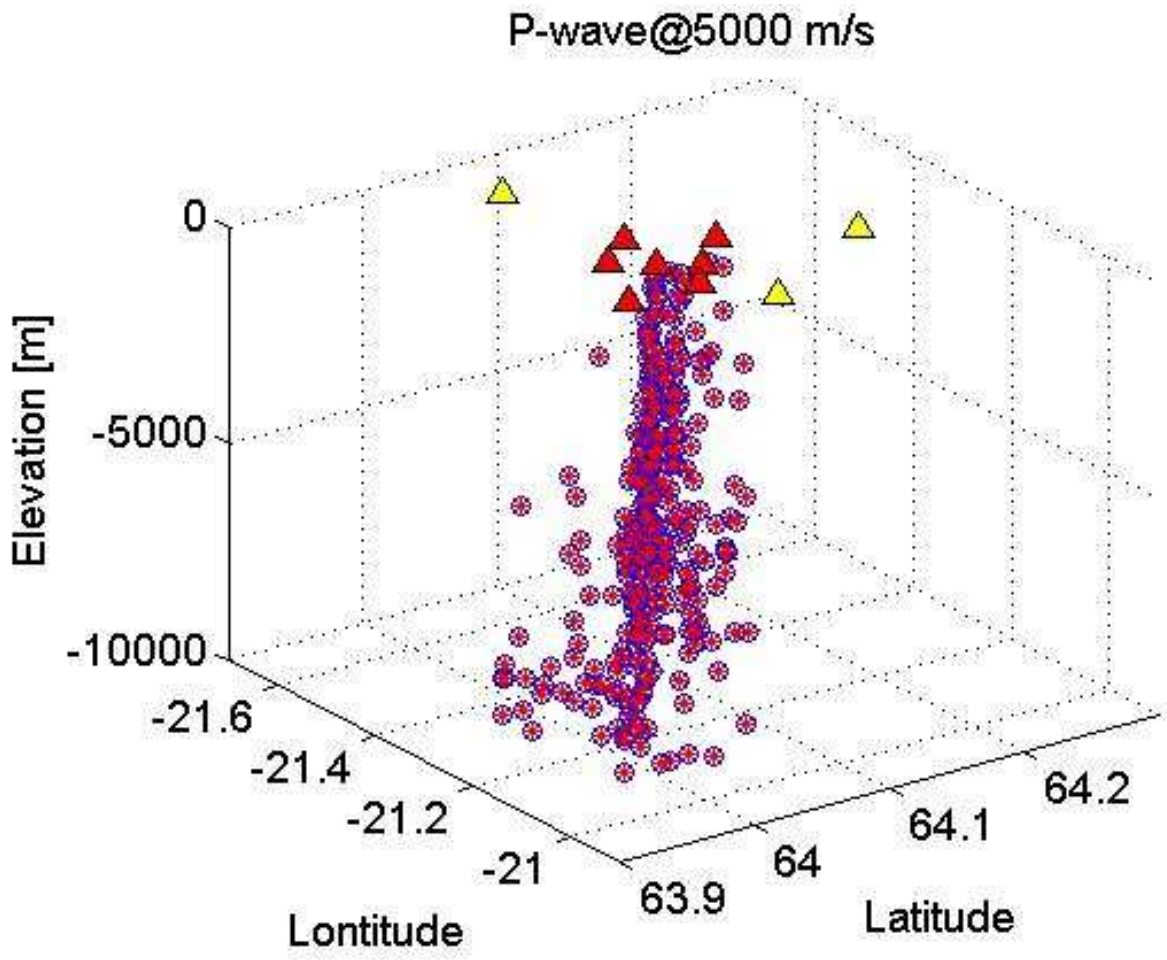

Figure 8: Locations obtained from the search grid inversion using P- arrival times and a constant velocity model of 5000 $\mathrm{m\,s^{-1}}$. View from the South-East above the network. Stations locations at surface indicated with triangles.

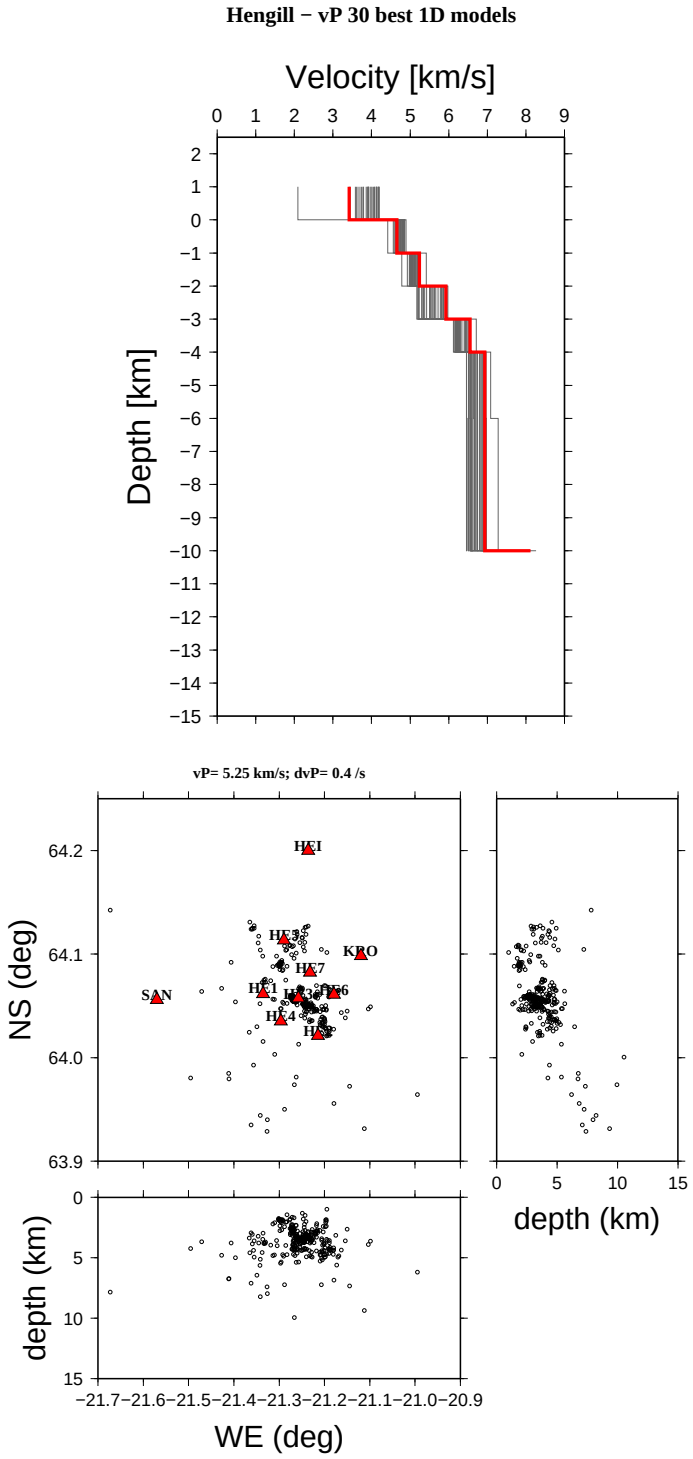

Figure 9: Inverted 1-D v_P model using P- and S-waves arrival times. The *a priori* locations are taken from the preliminary inversion (Figure 8). Left: inverted P-wave velocity 30 models with lower RMS; best model (lowest RMS) drawn with a thick line. Right: Epicenters and 2 vertical cross-sections (NS and SW) projections of all 339 hypocenters. Triangles: IGET network and SIL stations locations.

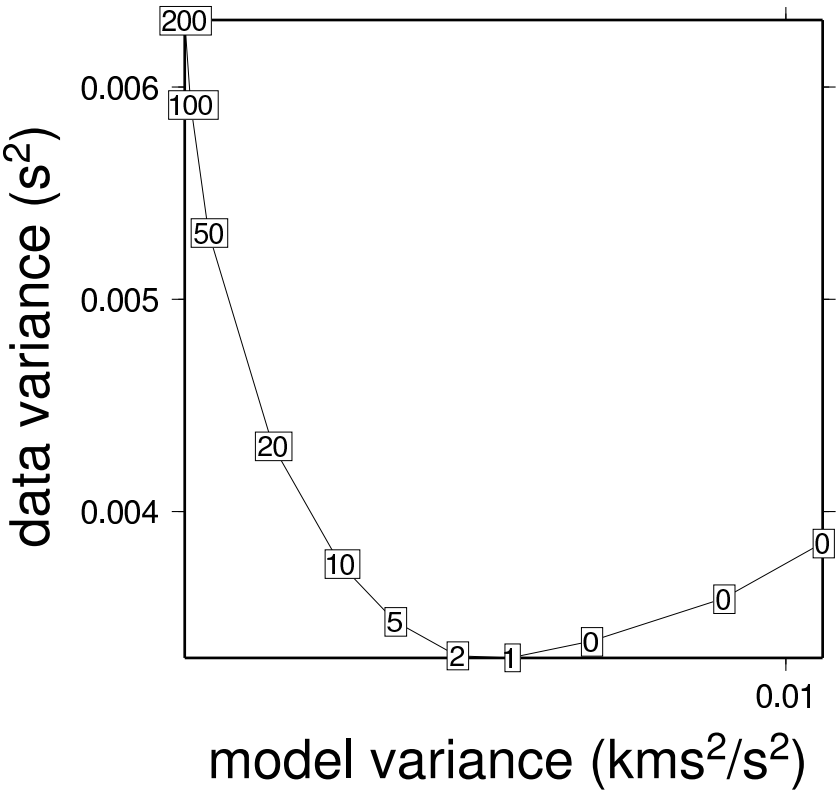

Figure 10: Trade-off curve of the damping between the data variance and model variance for the case of 3-D vP inversion sampled every 2 km. The damping parameter value chosen in this case will be 2.

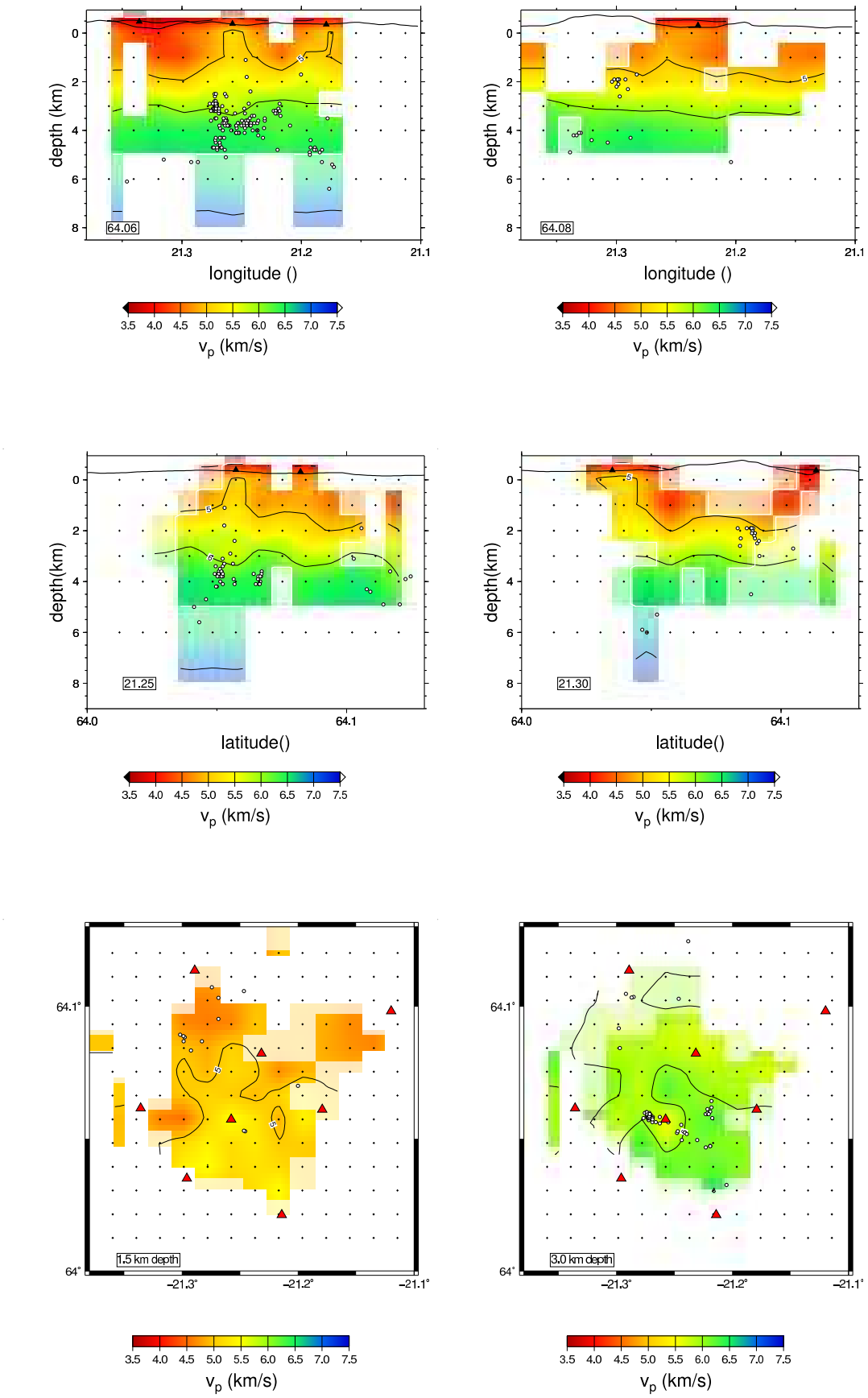

Figure 11: P-wave velocity 3-D tomography inversion at Hengill geothermal system using a grid of 1 km. Black triangles represent station locations at the surface indicated by a thick black line. White circles represent earthquake location within a -0.5/+0.5 degree range from the position of the cross-section and slice. (top)

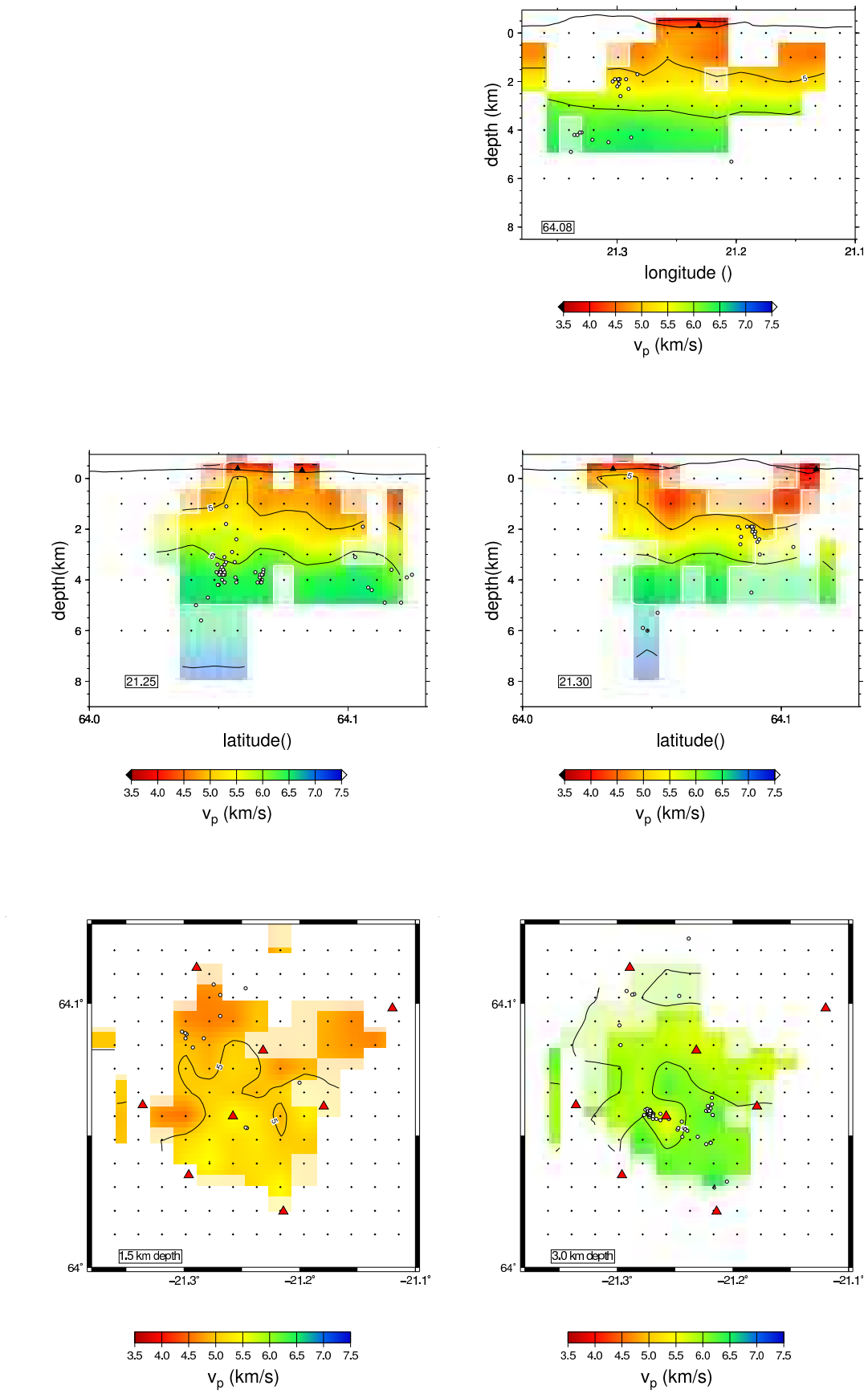

Figure 12: v_P/v_S ratio 3-D tomography inversion at Hengill geothermal system using a grid of 1 km. Black triangles represent station locations at the surface indicated by a thick black line. White circles represent earthquake location within a -0.5/+0.5 degree range from the position of the cross-section and slice. (top)